https://doi.org/10.5194/wes-2024-2
Preprint. Discussion started: 27 February 2024

The Effects of Wind Farm Wakes on Freezing Sea Spray in the Mid-Atlantic Offshore Wind Energy Areas

David Rosencrans[1,2], Julie K. Lundquist[1,2,3], Mike Optis[2,4], and Nicola Bodini[2]

[1]Department of Atmospheric and Oceanic Sciences, University of Colorado, Boulder, 80303, USA
[2]National Renewable Energy Laboratory, Golden, 80401, USA
[3]Renewable and Sustainable Energy Institute, Boulder, 80303, USA
[4]Veer Renewables, Courtenay, V9N 9B4, Canada

Correspondence to: David Rosencrans (David.Rosencrans@Colorado.edu)

Abstract

The U.S. is expanding its wind energy fleet offshore where winds tend to be strong and consistent. In the mid-Atlantic, strong winds, which promote heat transfer and wind-generated sea spray, paired with cold temperatures can cause ice on equipment when plentiful moisture is available. Near-surface icing is induced by a moisture flux from sea spray, which poses a risk to vessels and crews. Ice accretion aloft occurs when liquid precipitation is present and can reduce turbine blade performance and introduce extra load and fatigue on the turbine. Thus, it is crucial to understand the icing hazard across the mid-Atlantic. We analyze Weather Research and Forecasting model numerical weather prediction simulations at coarse temporal resolution over a 20-year period to assess freezing events over the long-term record and at finer granularity over the 2019–2020 winter season to identify the post-construction turbine impacts. Over the 2019–2020 winter season, results suggest that sea-spray–induced icing can occur up to 66 hours per month at 10 m at higher latitudes. Freezing events during this season typically occur during cold air outbreaks, which are the introduction of cold continental air over the warmer maritime surface and last a total duration of 253 hours. Over the 20-year period, all cold air outbreak events coincide with freezing conditions, although not all freezing events are cold enough to signify a cold air outbreak. Further, we assess the impacts of wind plant installation on icing using the fine-scale simulation data set. Wakes from large wind plants reduce the wind speed, which mitigates the chance for freezing. Conversely, the near-surface turbine-induced introduction of cold air in frequent wintertime unstable conditions enhances the risk for freezing. Overall, the turbine–atmosphere interaction causes a net mitigation of freezing hours within the wind plant areas, with a reduction up to 17 hours at 20 m in January 2020.

1 Introduction

The offshore wind energy industry is undergoing rapid growth to supply emissions-free energy to the electrical grid. Across the mid-Atlantic outer continental shelf (OCS), the installed capacity could reach 30 GW by 2030 (White House, 2021). Capacity expansion into relatively cold offshore regions will subject turbines to harsher wintertime conditions, which necessitate an understanding of the hazards that marine icing poses to offshore wind turbines, service vessels, and crew safety.

https://doi.org/10.5194/wes-2024-2
Preprint. Discussion started: 27 February 2024

Ice accretion reduces the aerodynamic efficiency of the turbine blade, which hinders energy capture and annual energy production (Battisti et al., 2006; Kraj and Bibeau, 2010; Wei et al., 2020). Ice can remain on the rotors even after freezing conditions end, as slow natural processes such as ice shedding and melting extend the limitation to energy yield (Gao and Hong, 2021). Some observations indicate that excessive icing can reduce torque enough that blade rotation stops entirely, causing up to 80 % reduced power production for a single turbine (Gao and Hu, 2021). Investigating a 2050 future capacity expansion scenario, Novacheck et al. (2021) found that onshore icing events could reduce wind energy generation by 7 % and 10 % over two case-study events using 65 % variable renewable energy penetration. For this scenario, Minnesota and Wisconsin would experience 75 % reduced wind energy generation during a daylong case study period, causing reliance on ramped up local gas generation and interregional transmission to meet the load. Faster winds in cold air outbreaks (CAO) enhance wind-energy supply during high-load cold-weather events, although the combination of cold temperatures and slow wind speeds following frontal passage pose severe challenges for utility grid planners. While turbine blade icing is well studied (Martini et al., 2021; Contreras Montoya et al., 2022), icing near the turbine base is not. Some turbines have icing detection and mitigation technology included at added cost, although current strategies need improvement (Madi et al., 2019).

The leading causes for low-level offshore icing are wave impact and wind induced sea spray (Dehghani-Sanij et al., 2017). Sea spray provides nuclei for ice clouds at high latitudes where airborne dust is sparse, being lofted by bursting bubbles and droplets from white-capped waves (Russell, 2015; Dehghani-Sanij et al., 2017). Ice accumulation from spray raises the center of gravity of ships, which can cause loss of stability and lead to capsizing (Guest and Luke, 2005). Ice accumulation is believed to have caused the recent losses of three ships, including 1) the *Destination*, which sank near St. George Island, Alaska in 2017 (Destination likely sank after accumulating ice in heavy freezing spray, report says, 2023); 2) the *Scandies Rose*, which sank southeast of Kodiak, Alaska, in 2019 (NTSB announces the probable cause of the sunken Scandies Rose, 2023); and 3) the *Onega*, which sank in the Barents Sea in 2020 (Icing believed to cause sinking of fishing boat in Barents Sea, 17 missing, 2023). To mitigate ice-induced accidents, inclement weather forecasts are furnished for coastal waters. A Coastal Waters Forecast, delivered by the National Weather Service, will contain a "freezing spray advisory" if freezing water droplets can accumulate on vessels due to a combination of sea surface temperature (SST), wind speed, air temperature, and vessel motion (Glossary - NOAA's National Weather Service, 2023). At rates greater than 2 cm h^{-1}, the advisory becomes a "heavy freezing spray watch".

Wind turbines can modify the amount and severity of freezing conditions via competing effects. Enhanced turbulence caused by spinning blades transports temperatures (either warmer or colder) from aloft to lower altitudes within the rotor-swept region or near the surface. In stable stratification, warmer potential temperatures are transported downward, which introduces a near-surface warming effect, and vice versa in unstable conditions (Fitch et al., 2013; Rajewski et al., 2013; Xia et al., 2016; Siedersleben et al., 2018; Tomaszewski and Lundquist, 2020). However, recent research suggests taller turbines may reverse this phenomenon (Golbazi et al., 2022). As the winter months feature more frequent unstable stratification along the U.S. East Coast (Bodini et al., 2019), turbine-induced

https://doi.org/10.5194/wes-2024-2
Preprint. Discussion started: 27 February 2024

eawe european academy of wind energy
Open Access WIND ENERGY SCIENCE DISCUSSIONS

cooling may increase the potential for near-surface icing. In contrast, turbines harness momentum from the flow, which reduces the downwind wind speed (Nygaard, 2014; Platis et al., 2018; Schneemann et al., 2020). A reduction in wind speed conversely reduces the potential for icing (Dehghani-Sanij et al., 2017). Thus, it is crucial to understand how large-scale wind deployment across the mid-Atlantic will modify the regularity and intensity of freezing conditions.

Herein, we employ numerical weather prediction modeling to quantify the baseline offshore icing risk and the wind plant post-production effects. Section 2 outlines the modeling setup and discusses the techniques for discerning freezing events and cold air outbreak. Section 3 reports results for the spatiotemporal icing risk, causal factors, and the adjustments by wind plants. Section 4 offers concluding remarks and discussion.

2 Methods

2.1 NOW-23

We explore annual variability of freezing conditions using the 2023 National Offshore Wind (NOW-23) dataset (NREL, 2020; Bodini et al., 2023). This dataset provides an offshore wind resource spanning all offshore regions of the United States at 5 min resolution for up to 22 years. For the mid-Atlantic region, NOW-23 was validated against observations from three ZephIR ZX300M floating lidars (Pronk et al., 2022). We acquire model output at an hourly temporal resolution for the 20-year period from 01 January 2000 to 31 December 2020. NOW-23 employs the Weather Research and Forecasting (WRF) model (Powers et al., 2017) version 4.2.1. A parent domain feeds into an inner nested domain with horizontal grid resolutions of 6 km and 2 km, respectively. Both domains have a vertical grid resolution of 5 m near the surface with stretching to 45 m aloft, using 61 vertical levels up to a 50 hPa top. The European Centre for Medium Range Weather Forecasts 5 Reanalysis (ERA5) dataset supplies hourly initial and boundary conditions at a 30 km resolution to WRF (Hersbach et al., 2020). NOW-23 employs the MYNN2 planetary boundary layer and surface layer (Nakanishi and Niino, 2006) schemes, eta microphysics (Ferrier et al., 2002), the Noah Land Surface Model (Tewari et al., 2004), the rapid radiative transfer model for shortwave and longwave radiation (Iacono et al., 2008), and the Kain–Fritsch cumulus parameterization (Kain, 2004) in the outmost domain only.

2.2 NOW-WAKES

We explore the seasonal variability and impacts of wind plants on icing conditions using high-fidelity numerical weather prediction simulations over the period 01 September 2019 to 31 August 2020. These validated WRF version 4.2.1 simulations are described in detail in Rosencrans et al. (2023) but are summarized here for the reader's convenience. This period is chosen for the availability of lidar measurements for validation of the wind speed profile. A parent domain hosts an inner nest with horizontal grid resolutions of 6 km and 2 km, respectively (Figure 1). Both domains have a vertical grid resolution of 10 m near the surface with stretching aloft, using 54 vertical levels up to a 50 hPa top. The inner domain outputs data at an instantaneous history file frequency of 10 minutes. Constant time steps are set to 18 s and 6 s in the outer and inner domains, respectively. Initial and boundary conditions are also supplied by the hourly 30 km ERA5 dataset (Hersbach et al., 2020). Lower boundary conditions

https://doi.org/10.5194/wes-2024-2
Preprint. Discussion started: 27 February 2024

are provided as SST by the UK Met Office Operational Sea Surface Temperature and Sea Ice Analysis dataset (Donlon et al., 2012) and show good agreement during validation against mid-Atlantic bight buoys (Redfern et al., 2023). Physics parameterizations include the MYNN2 planetary boundary layer and surface layer (Nakanishi and Niino, 2006), the Noah Land Surface Model (Niu et al., 2011), the New Thompson microphysics (Thompson et al., 2008), the rapid radiative transfer model for longwave and shortwave radiative transfer (Iacono et al., 2008), and the Kain–Fritsch Cumulus (Kain, 2004) schemes. The Kain–Fritsch cumulus parameterization applies to the parent domain only.

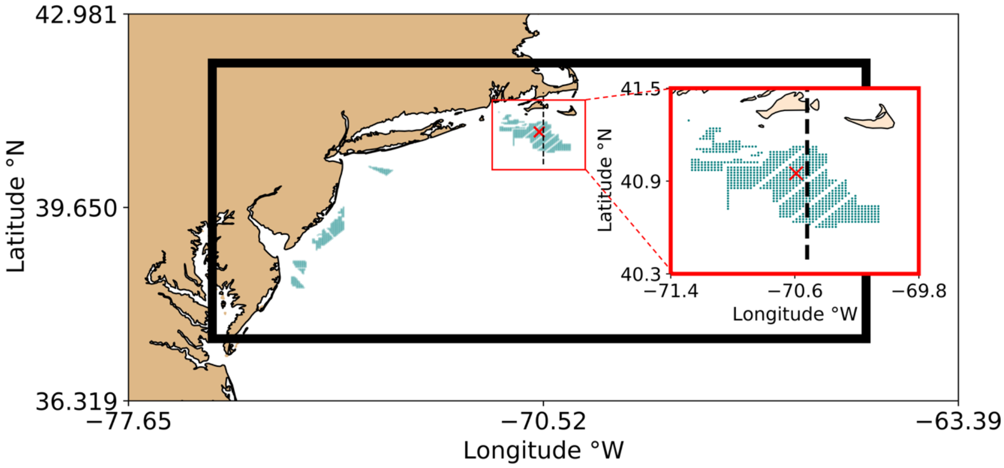

Figure 1. Modeling domains. The entirety of the outer domain with inner domain is shown, outlined by the black rectangle. The red square is zoomed in on the Rhode Island–Massachusetts (RIMA) block to enhance visibility. Turbines are shown as teal dots. The red "X" indicates the point of interest (POI) where time series are acquired. The dashed black line is a cross section extending through the RIMA block.

We incorporate the effects of wind turbines using the WRF wind farm parameterization (WFP) (Fitch et al., 2012). WFP simulations feature wind plant layouts of the lease areas and include 1,418 turbines (Figure 1, Table 1). The WFP incorporates the effects of turbines by implementing a drag-induced deceleration of wind flow and an addition of turbulence at model levels intersecting the rotor area. We execute WFP simulations adding both 0 % and 100 % turbulent kinetic energy (TKE) (Rosencrans et al., 2023), although a smaller value of 25 % agrees better with neutrally stratified large-eddy simulations (Archer et al., 2020). The differences in icing results between 0 % and 100 % added TKE are slight, so we report those from 100 % added TKE only. This work utilizes 12 MW GE Haliade wind turbines with a 138 m hub height and 215 m rotor diameter, which is scaled by Beiter et al. (2020) from a 15 MW reference turbine. We carry out separate simulations using both no wind farms (NWF) and wind farms (WFP) for the full year-long period from 01 September 2019 to 31 August 2020 (Table 1).

https://doi.org/10.5194/wes-2024-2
Preprint. Discussion started: 27 February 2024

Table 1. List of simulations characterized by turbine characteristics.

Simulation Type	Turbine Type	Period	Added TKE	# Turbines
No Wind Farms (NWF)	N/A	09/2019–08/2020	N/A	0
Wind Farm Param. (WFP)	12 MW	09/2019–08/2020	0 %	1,418
Wind Farm Param. (WFP)	12 MW	09/2019–08/2020	100 %	1,418

2.3 Freezing hours detection

Ice accretion occurs when supercooled water freezes upon contact with objects. The largest contributions to sea spray icing are provided by the bursting of bubbles and advection of spray from white-capped waves (Dehghani-Sanij et al., 2017). Further aloft, supercooled water can be introduced by liquid precipitation and fog. In the presence of moisture, there are three key variables that dictate offshore freezing conditions: wind speed, SST, and air temperature (Overland et al., 1986; Overland, 1990; Guest and Luke, 2005; Dehghani-Sanij et al., 2017; Line et al., 2022).

We define input freezing conditions following the most liberal thresholds defined by the latter studies (Guest and Luke, 2005; Dehghani-Sanij et al., 2017; Line et al., 2022), which produce more freezing events, to compensate for a negative wind speed bias in unstable stratification (Rosencrans et al., 2023), which mitigates freezing occurrence. These criteria require 1) wind speeds in excess of 9 m s^{-1}, 2) air temperatures below −1.7° C, and 3) SST less than 7° C. The skin temperature (WRF output variable "TSK") is used because the SST field inherits coarse blocks of missing data around coastlines from the ERA5 dataset. The resulting spatial maps are masked by the land use (WRF output variable "LU_INDEX") to ensure freezing conditions over land are not counted. The number of 10 min timestamps where these criteria are met each month are recorded for all simulations.

Sea spray–induced icing can affect structural integrity, blade aerodynamics, and crew safety. As sea spray often lofts to between 5 and 20 m above sea level (Dehghani-Sanij et al., 2017), we detect possible icing conditions at the lowest model level of 10 m and at 20 m. We further consider riming conditions at the 138 m hub height by including an additional criterion for the presence of liquid rainwater, as precipitation-induced ice can generate a considerably higher ice accretion rate than fog-induced icing (Gao and Hong, 2021).

2.4 Ice accumulation rate

A predictability function assesses the likelihood for freezing in the presence of sea spray. We assess the predictability of icing conditions at the point of interest (POI) in the Rhode Island/Massachusetts (RIMA) block (Figure 1) separately from the NOW-WAKES and the NOW-23 datasets. The predictability (PPR) for sea spray–induced ice formation follows:

$$PPR = \frac{V_a(T_f - T_a)}{1 + 0.4(T_s - T_f)} \quad (1)$$

https://doi.org/10.5194/wes-2024-2
Preprint. Discussion started: 27 February 2024

where V_a is the wind speed, T_f is the temperature threshold of −1.7° C, T_a is the air temperature, and T_s is the SST (Guest and Luke, 2005; Overland et al., 1986; Overland, 1990). A humidity variable is not present in Eq. (1) due to the assumption that sea spray introduces a constant source of moisture during fast winds, that of which is required for nonzero PPR. A group of successive timestamps with nonzero PPR are considered the same event. Separate flagged timestamps occurring within 24 hours of each other span the same synoptic regime (Winters et al., 2019), and so the entire duration between the two flagged timestamps is considered one event.

Table 2. Icing rate by PPR. Rows delineate icing predictability (PPR), icing class, and ice accretion rate. Columns delineate the icing rate per PPR range. From Guest and Luke (2005).

PPR	<0	0–22.4	22.4–53.3	53.3–83.0	>83.0
Icing Class	None	Light	Moderate	Heavy	Extreme
Icing Rate [cm h^{-1}]	0	<0.7	0.7–2.0	2.0–4.0	>4.0

The magnitude of PPR can determine the rate of ice accretion (Table 2). The ice accretion rates are a general guideline developed for 20 to 75 m vessels; specific rates depend on the type of ship, its load, and its handling characteristics (Guest and Luke, 2005). For instance, a larger ship requires faster winds and taller waves for sea-spray–induced ice to accumulate on a higher deck but is more vulnerable to the prevailing wind direction due to reduced maneuverability. It is not known how these icing rates would apply to wind turbines or to the vehicles used to access offshore wind turbines.

2.5 Cold air outbreak detection

Freezing conditions can be stimulated by the advection of cold continental air over a warmer maritime surface. The resulting temperature profile induces instability, which causes filamentary convective rolls that align to make cloud "streets" with parallel columns of ascending and descending air that transform into open convective cells further offshore (Geerts et al., 2022). An approach proposed by Vavrus et al. (2006) identifies a CAO by the magnitude and duration of anomalous air temperature, which we apply at the POI (Figure 1). This strategy requires that the near-surface temperature be at least 2 standard deviations below the wintertime average following Eq. (2):

$$T < \bar{T} - 2(\sigma) \tag{2}$$

where T is the 10 m temperature, $\bar{T}$ is the average 10 m temperature during the wintertime period, and σ is the standard deviation. The wintertime period spans November through March at a 10 min frequency to account for all non-zero-freezing predictability events. Again, successive timestamps with detected CAO are considered a single event, and separate events occurring within a 24 h span are conglomerated into the same event.

2.6 Atmospheric stability

Turbulence from wind turbines modifies the near-surface temperature based on the atmospheric stability or stratification. We calculate the modeled atmospheric stability using the Obukhov Length (L) (Monin and Obukhov,

https://doi.org/10.5194/wes-2024-2
Preprint. Discussion started: 27 February 2024

1954) (Eq. 3), which delineates the height above the surface at which buoyant turbulence equals mechanical shear production of turbulence, at a point centered on the RIMA block of lease areas:

$$L = -\frac{u_*^3 \overline{\theta_v}}{\kappa g \left(\overline{w' \theta_v{}'} \right)} \tag{3}$$

where u_* (UST in WRF output) is the friction velocity, θ_v is the virtual potential temperature, κ is the von Kármán constant of 0.4, g is gravitational acceleration of 9.81 m s^{-1}, and $\overline{w'\theta_v{}'}$ (HFX in WRF output) is the surface dynamic heat flux converted into kinematic heat flux. Negative lengths between 0 m and −500 m imply unstable stratification due to a positive heat flux (Archer et al., 2016). Conversely, lengths between 0 m and 500 m imply stable stratification due to a negative heat flux. Lengths approaching negative or positive infinity imply neutral stratification, as buoyancy is no longer a dominating factor. Each 10 min timestamp from the NWF run is assigned a stability classification from November 2019 to March 2020.

3 Results

3.1 Spatial variability of freezing conditions

The percentage of occurrence of freezing conditions exhibits regional variability. The commonality of freezing increases toward higher latitudes and near the coast where cold continental air advects over the ocean during the winter (Figure 2). In general, the spatial icing pattern during the 2019–2020 winter season (Figure 2a) matches well with the pattern over the 20-year period (Figure 2b). Freezing conditions shadow the mid-Atlantic coast but occur less often along the New Jersey Bight where wind speeds decrease and temperatures warm. The commonality of freezing conditions extends furthest offshore southeast of Nantucket and enhances in the Long Island Sound; both regions feature local minima in mean January 2020 SST less than 5° C. To the north, the cyclonic current in the Gulf of Maine transports cold surface water southward. East of Cape Cod, this current bifurcates, and a branch feeds cold fresh water into the mid-Atlantic. Predominant northerly winter winds instigate onshore Ekman transport towards the coast, which is favorable for downwelling (Shcherbina and Gawarkiewicz, 2008b). However, downwelling is not always supported, as the mixed layer stratification is dominated by salinity (Shcherbina and Gawarkiewicz, 2008a), leaving a cold pool near the surface.

https://doi.org/10.5194/wes-2024-2
Preprint. Discussion started: 27 February 2024

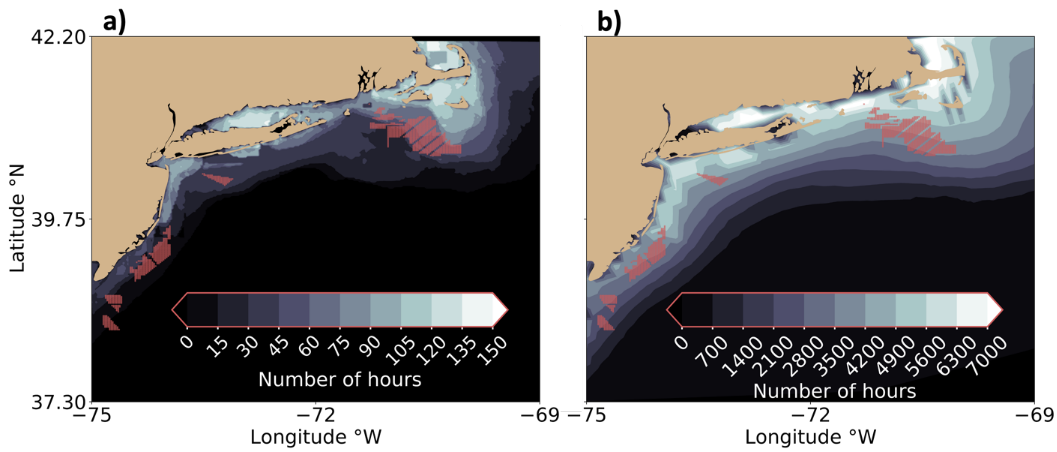

Figure 2. The number of hours freezing conditions occur during (a) the November 2019 to March 2020 period at 10 m in NWF and (b) the November to March period from 2000 to 2020 in NOW-23. Lighter contouring indicates more freezing hours. Red dots represent turbine locations.

Freezing conditions exhibit seasonal variability in NWF, starting at 0 hours in November, increasing through the winter, and falling to 0 again by April at all heights (Figure 3 and Figure. A1–A3). At the 10 m altitude, freezing conditions occur most often in January, up to 66 hours, with an offshore spatial extent of 57,420 km^2, or roughly 12 times the area of the wind plants. At 20 m, freezing conditions also occur most often in January, up to 70 hours, covering a total area of 61,924 km^2, or roughly 13 times the area of the wind plants. The 20 m height experiences more freezing hours than the 10 m height because average wind speeds are at least 0.25 m s^{-1} faster around Nantucket, Cape Cod, and the Long Island Sound. The 138 m hub height has a smaller maximum of 29 hours during January in the Gulf of Maine, with a band extending south from Cape Cod, posing no threat to the lease areas (Figure A3). Although wind speeds increase aloft, the regularity of liquid water is not as consistent, as is near-surface sea spray.

https://doi.org/10.5194/wes-2024-2
Preprint. Discussion started: 27 February 2024

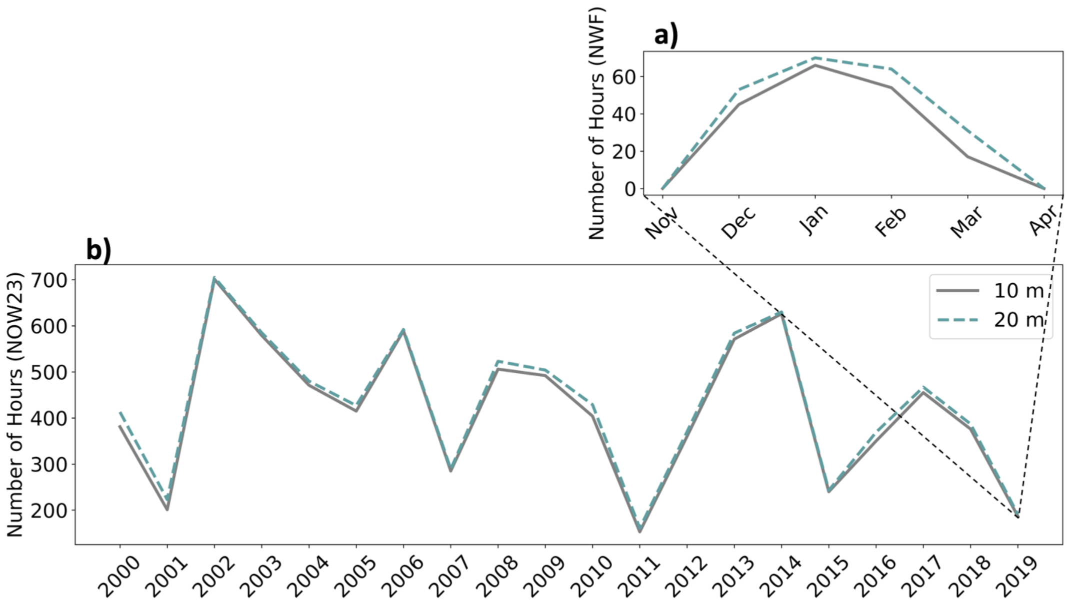

Figure 3. The maximum number of freezing hours over the OCS (a) seasonally and (b) annually from 2019 to 2020.

The 2019–2020 winter season was the mildest compared to other winters (Figure 3b). This winter season had the fewest number of freezing hours compared to other winters over the 20-year period, reaching 182 hours in NWF or 187 hours in NOW-23 at 10 m. At 20 m, the 2019–2020 winter season contains 218 hours in NWF or 191 hours in NOW-23. The greatest number of freezing hours occurs during the 2002–2003 season, with 701 total hours at 10 m and 705 hours at 20 m. While the 20 year slope shows a decrease, it is not statistically significant using the Mann–Kendall (M–K) test (Hussain and Mahmud, 2019). P-values for the maximum number of hours (found across the OCS) (Figure 3b) and for the number of freezing hours at the POI (Figure 1) are 0.20 and 0.12, respectively. We additionally applied the seasonal M–K test (Hirsch et al., 1982) to account for upward and downward trends throughout the year on monthly mean PPR, monthly maximum PPR, and the monthly total number of freezing hours at the POI. Neither test returned a statistically significant trend.

3.2 Freezing conditions and cold air outbreak

Investigating all events with a non-zero freezing PPR at the POI (Figure 1) reveals similar synoptic trends. We identify seven events with freezing sea spray (FSS) conditions with a total duration of 253 hours from November 2019 to March 2020. All times during the 2019–2020 winter period with nonzero PPR contain light ice accumulation of less than 0.7 cm h^{-1} (Table 2). During each FSS event, higher relative pressure resided to the southwest throughout the Great Plains, Appalachia, or the Great Lakes with lower relative pressure to the northeast around Novia Scotia and Newfoundland. The largest pressure gradient forces occurred during the two January events of up to $4x10^{-3}$ Pa m^{-1}, or roughly 4 times the pressure gradient force required for a 10 m s^{-1} geostrophic

https://doi.org/10.5194/wes-2024-2
Preprint. Discussion started: 27 February 2024

wind in the midlatitudes (Parish et al., 2007). Most events feature either an outflow boundary or cold front. This pressure regime directs quasi-geostrophic flow near the surface toward the southeast, introducing cold continental air offshore. During the winter, the prevailing wind direction is northwesterly across the mid-Atlantic OCS (Bodini et al., 2019) because regions of land mass feature higher surface pressure than the surrounding ocean and the Bermuda High retreats to the east.

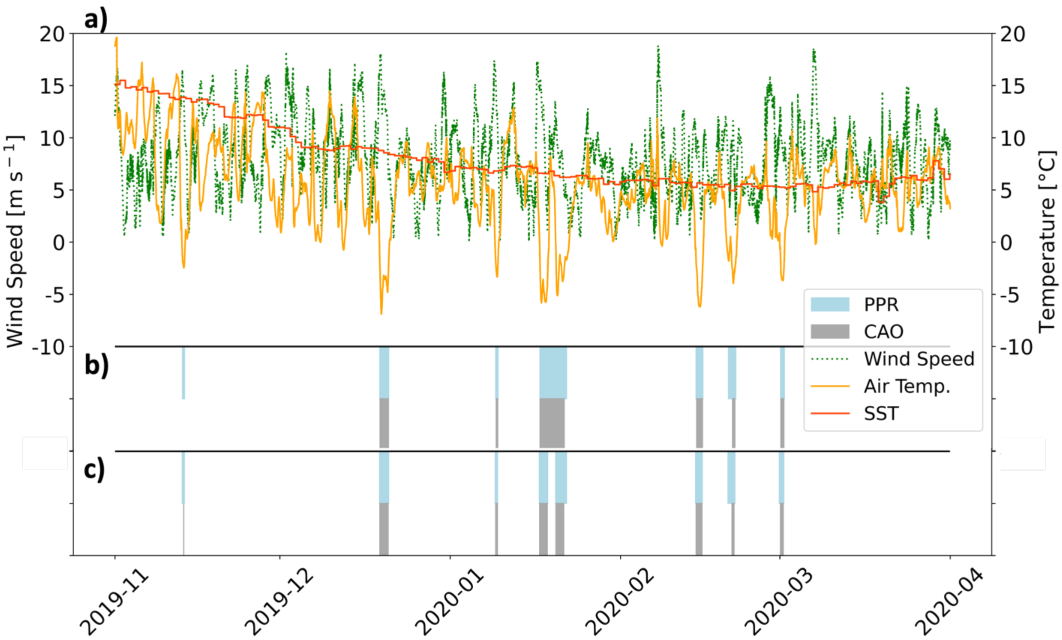

Figure 4. (a) Time series of wind speed (green dotted), 10 m air temperature (orange), and SST (red) from November 2019 to April 2020 at the downwind edge of Vineyard Wind (Figure 1). Light-blue shading indicates the duration of nonzero PPR, and gray shading indicates the duration of detected CAO from (b) NWF and (c) NOW-23.

Most offshore freezing events coincide with CAO. We detect six CAO events in NWF with a total duration of 200 hours (Figure 4b). The typical durations of CAO events are 3 hours shorter than FSS, with 78.9 % of flagged FSS timestamps having CAO present. Overall, six of the seven FSS events occur in conjunction with a CAO (Figure 4b), with November air temperatures not cold enough to be flagged as CAO candidates. We note that in NWF, all seven FSS events coincide with CAO at the northeast edge of the RIMA block which is nearer to the introduction of cold continental air.

Common between events are fast wind speeds and cold 10 m air temperatures; SST plays a secondary role for its weak variability (Figure 4a). The average wind speed during FSS events is 10 m s^{-1} with gusts exceeding 15 m s^{-1} during four events. Nonzero PPR does not occur until after the wind speed peaks, when cold air temperatures

https://doi.org/10.5194/wes-2024-2
Preprint. Discussion started: 27 February 2024

sweep in, averaging minimum temperatures of −5° C (Figure 4a). This wind speed–temperature dynamic poses challenges for grid planners because wind energy generation reduces during periods of peak heating load.

Over the 2019–2020 winter in the NOW-23 dataset, eight total events are flagged as candidates for FSS because the longest event in January 2020 (Figure 4b) is split among two separate events; all eight events have a corresponding CAO (Figure 4c). Over the 20-year period, *all* CAO events occur in conjunction with an FSS event (positive PPR). However, many FSS events occur without CAO present meaning that CAO is only one of the drivers, and large interannual variability can exist. For instance, while 97 % of CAO timestamps concur with FSS during the 2011–2012 season, only 9 % do during the 2013–2014 season.

The 2019–2020 winter ice accumulation rate is similar to other winters. The average PPR during freezing events from 2019 to 2020 is 4.3, which corresponds to a light ice accumulation rate of less than 0.7 cm h^{-1} (Table 2). Over the 20-year period, the average PPR among events is 8.1, which corresponds to the same accumulation rate. The 2003–2004 winter period features the greatest mean PPR of 15.7, which also corresponds to a light ice accumulation rate. During this period, a moderate risk for icing occurred 18 % of the time, and a heavy risk occurred 3 % of the time, corresponding with icing rates between 0.7–2.0 cm h^{-1} and 2.0–4.0 cm h^{-1}, respectively, and possibly triggering heavy freezing spray watches in the NWS advisory.

3.3 Modifications by wind plants

Icing is more probable in cold temperatures. In unstable conditions, which occur 64 % of the time from November 2019 through March 2020 in NWF assessed at the POI, wind turbines introduce near-surface cooling, which could increase the likelihood of icing. For instance, mean cooling and warming during unstable conditions reach magnitudes up to −0.041 K at the surface and 0.022 K within the rotor-swept region, respectively, along a cross section extending through the RIMA block (Figure 1, Figure 5b). During stable conditions, which occur 25 % of the time from November through March, cooling aloft reaches up to −0.34 K, and near-surface warming reaches 0.26 K (Figure 5a). Near-surface cooling exists adjacent to the wind plant cluster.

https://doi.org/10.5194/wes-2024-2
Preprint. Discussion started: 27 February 2024

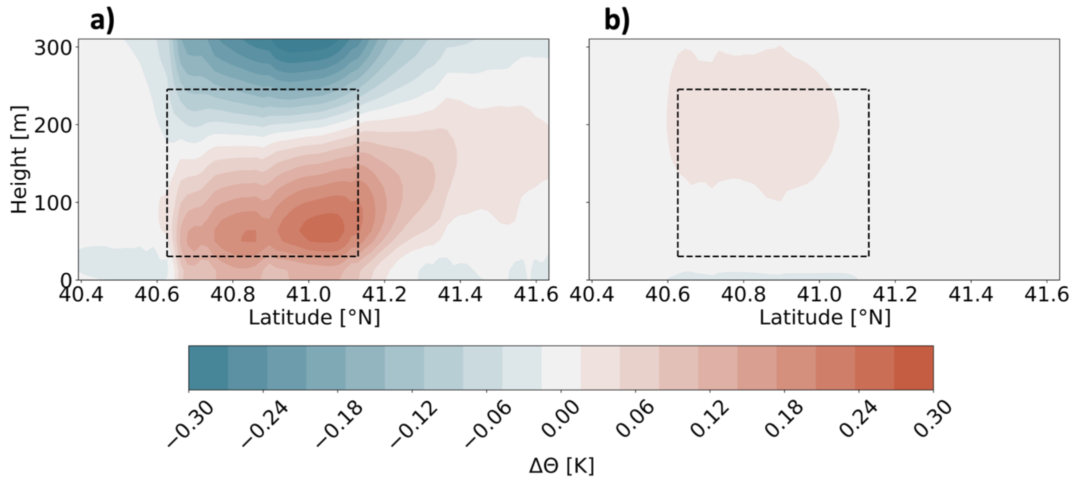

Figure 5. The mean (WFP-NWF) potential temperature difference during (a) stable stratification and (b) unstable stratification, from November 2019 to March 2020. The cross section spans the RIMA block of lease areas (Figure 1). Red contouring indicates warming, and blue indicates cooling. Dashed lines outline the wind plant area and rotor-swept region.

Conversely, the reduction of wind speeds in the wake modifies the chance for icing. In stable conditions, the wake wind speed deficit is largest, reaching −1.4 m s^{-1} near the top of the rotor-swept plane, reducing the chance for freezing. Because vertical motion is suppressed in stable stratification, winds increase and flow around and under the wind plant area (Figure 6a), reaching a subtle enhancement near the surface of 0.17 m s^{-1}. In unstable stratification, available buoyant turbulence promotes mixing which transports momentum from above the rotor-swept region down to within the wake. The injection of momentum allows wake wind speeds to recover, leaving a smaller maximum averaged wake deficit of −0.57 m s^{-1} (Figure 6b). There is no enhancement of wind speeds adjacent to the RIMA block along the cross section in unstable conditions.

https://doi.org/10.5194/wes-2024-2
Preprint. Discussion started: 27 February 2024

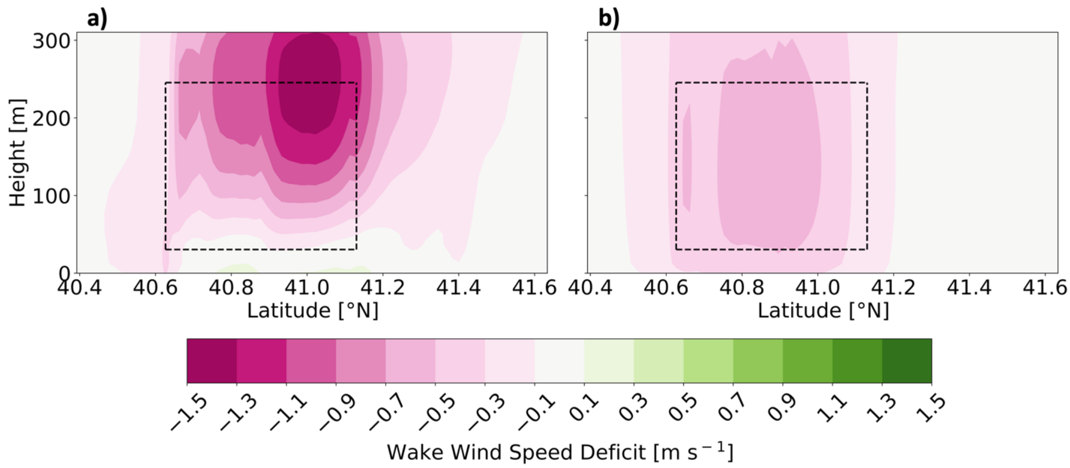

Figure 6. The mean (WFP-NWF) wind speed difference during (a) stable and (b) unstable stratification, from November 2019 to March 2020. The cross section spans the RIMA block of lease areas (Figure 1). Pink contouring indicates a wind speed reduction, and green indicates wind speed enhancement. Dashed lines outline the wind plant area and rotor-swept region. Note the very small enhancement of wind speeds near the surface in stable conditions.

Despite near-surface cooling, net freezing conditions occur less often when diagnosed using wind speed, air temperature, and SST criteria because of the wake wind speed reduction. At 10 m, the turbine–atmosphere interaction alters possible icing conditions the most in January and February, with a maximum reduction by 13 hours (Table 3). At 20 m, wind plants cause a reduction by up to 17 hours in January. In each case, the reduction in possible freezing conditions is spatially coincident with the wind plant areas (Figure 7). At the 138 m hub height, the change to the number of freezing conditions maximizes in December, with a reduction by 6 hours.

Table 3. The turbine-induced change in freezing hours by month and height.

Change in Number of Freezing Hours Throughout Domain						
	November	December	January	February	March	April
10 m	0	−2	−13	−13	−10	0
20 m	0	−4	−17	−16	−12	0
138 m	0	−6	−3	−3	−3	0

The introduction of wind turbines also increases the chance for freezing surrounding the wind plants, reaching maxima in March of 5 and 6 hours at 10 m and 23 m, respectively (Figure A4, Figure A5). Flow acceleration is present adjacent to the wake as winds deflect around the clusters (Stoelinga et al., 2022; Golbazi et al., 2022). However, freezing enhancement is isolated to a speckled pattern (Figure 7), does not coincide with the wind speed enhancement, and thus may result from numerical noise introduced by the WFP (Ancell et al., 2018; Lauridsen and Ancell, 2018). As modifications to the percentage of freezing conditions at the hub height are not spatially coincident with the lease areas or prevailing wind, these changes may also result from numerical noise (Figure A6).

https://doi.org/10.5194/wes-2024-2
Preprint. Discussion started: 27 February 2024

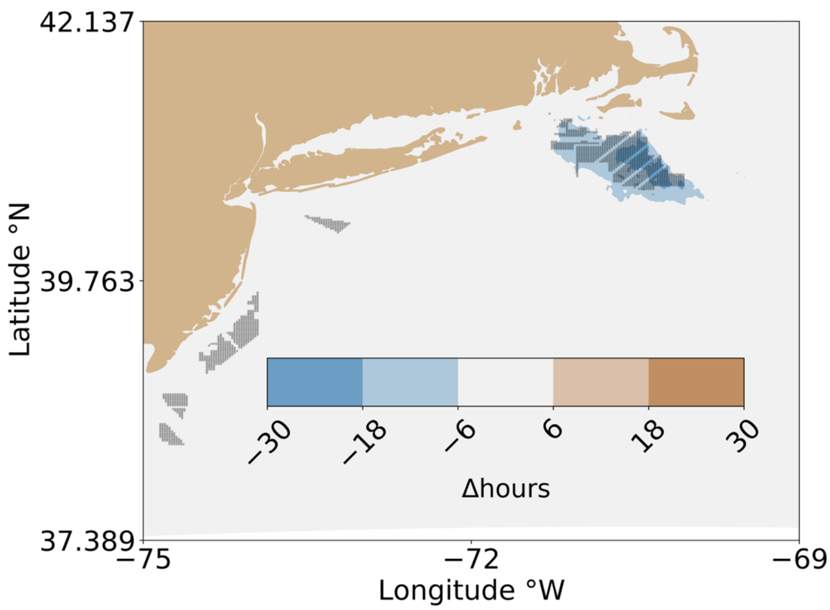

Figure 7. The (WFP-NWF) change in percentage of freezing hours at 10 m November 2019 to March 2020. Blue contours indicate a percentage reduction, and orange contours indicate a percentage increase.

Overall, the presence of wind turbines has a minimal impact to the number of hours freezing conditions occur by means of icing PPR at the POI. The duration of nonzero PPR over the November through March winter period increases by 3 hours, or from 253 to 256 hours total, at a point centered on the RIMA block. The total duration of CAO decreases by 1 hour, or from 200 hours to 199 hours, after the installation of wind plants. The total number of events (seven) does not change in the presence of wind turbines, and all flagged timestamps still cause light icing of less than 0.7 cm h^{-1}.

4 Conclusions

Here, we assess the threat of freezing conditions due to sea-spray icing and hub-height riming on wind turbines. The simulation study encompasses the mid-Atlantic Outer Continental Shelf based on a 20-year WRF dataset from 01 January 2000 to 31 December 2020 and another WRF dataset using year-long simulations from 01 September 2019 to 31 August 2020. In each case, we focus on the wintertime period from November through March. We consider the present icing risk from simulations with no wind farms (NOW-23, NWF) and assess the post-production adjustments by incorporating the effects of turbines (WFP) in a full buildout of the wind plant lease areas.

We detect seven events flagged for freezing sea spray conditions in NWF with a total duration of 253 hours during the November 2019 to March 2020 period. All times during the period with nonzero icing predictability

https://doi.org/10.5194/wes-2024-2
Preprint. Discussion started: 27 February 2024

(PPR) contain light ice accumulation of less than 0.7 cm h^{-1}, which is typical for the region as assessed from 2000 to 2020. Centered at the RIMA block of lease areas, six of the seven events have an associated CAO in NWF during the 2019–2020 winter, and all seven events have corresponding CAO at the northeast end of the block. In the NOW-23 dataset over the same period, eight total events are flagged, and all eight correspond with CAO. From 2000 to 2020, every CAO event has a corresponding freezing sea spray event, although not all freezing events have attendant CAO. Thus, offshore freezing may be forecast with reasonable fidelity through accompanying CAO, although other drivers exist. There is strong teleconnection between anomalous arctic sea level pressure sea level pressure and CAO, as 93 % of CAO events in the eastern U.S. contained an antecedent positive arctic sea level pressure anomaly a week in advance (Vavrus et al., 2006).

Freezing conditions exhibit spatial variability. The hazards intensify toward higher latitudes, near the land surface where cold air advects offshore, and by Nantucket and the Long Island Sound where SSTs are colder. Freezing conditions at the hub height from supercooled liquid water are less frequent. The icing hazard is greatest during January when wind speeds are fast and temperatures are cold. At 10 m in January, favorable conditions for icing occur up to 66 hours. At 20 m in January, the duration of icing conditions increases to 70 hours. Finally, at the hub height, freezing conditions occur for up to 29 hours in the Gulf of Maine and pose no risk to the lease areas. Overall, the 2019–2020 winter period is the mildest winter when considering the 20-year period. Although the 2019–2020 winter season has the fewest number of freezing hours, all winters contain light ice accumulation rates of 0.7 cm h^{-1}.

The introduction of large wind plants makes a small impact on the icing risk within the wind plant clusters. In wintertime unstable conditions, which occur 64 % of the time from November 2019 through March 2020, wind turbines introduce a mean near-surface cooling effect. Despite the enhanced freezing risk from supplementary cooling, slower wind speeds in the wake mitigate the hazard. Mean reductions in wind speed within the wakes reach up to −0.57 m s^{-1} in unstable conditions with an introduction of cooler air up to −0.041 K. As assessed using wind speed, air temperature, and SST criteria, the change in icing risk over the 2019–2020 wintertime period is a net reduction, by up to 13 hours at 10 m. At 20 m, mitigation reaches up to 17 hours. The alleviation by slower wind speeds is largest within the RIMA block of wind plants which contains the greatest number of turbines. When assessed using icing PPR centered on the RIMA block, the number of hours freezing conditions and CAO occur change by 3 and −1 hours, respectively. However, the 2019 through 2020 winter period is the mildest winter, so the introduction of wind plants may make more significant changes during harsher winters.

Future OCS winter storm frequency may differ due to climate change. For instance, warming Arctic temperatures, which reduce the meridional geopotential height gradient between the Arctic and midlatitudes, can weaken the jet stream. Slower zonal winds and more pronounced Rossby waves amplify the transport of extreme winter weather to the midlatitudes (Cohen et al., 2020). Future East Coast storm activity and temperature may experience modulations based on large-scale teleconnections such as El Niño and the North Atlantic Oscillation

(Hall and Booth, 2017). Further, Arctic amplification may increase the strength of teleconnection found between positive Arctic sea level pressure anomalies and CAO (Vavrus et al., 2006).

Finally, we assume that sea spray provides a consistent moisture flux at 10 and 20 m during fast wind conditions, that the droplet size of spray is homogeneous, and that the number distribution by height is constant. Future studies may benefit from coupling WRF with wave models, such as Wave Watch III (Tolman et al., 2019) and Simulating WAves Nearshore (SWAN Team, 2020) for precise modeling of wave induced sea spray and for current dynamics, such as stratified cold pooling around Cape Cod. New satellite methods are being developed to quantify occurrences of freezing sea spray (Line et al., 2022), and future developments should compare the FSS criteria to satellite observations of FSS.

5 Code and data availability

The dataset and files that support this work are publicly available. The ERA5 initial and boundary conditions can be downloaded from the ECMWF Climate Data Store at https://cds.climate.copernicus.eu/cdsapp#!/dataset/reanalysis-era5-pressure-levels?tab=form. Shapefiles including the bounds for wind energy lease areas are at https://www.boem.gov/renewable-energy/mapping-and-data/renewable-energy-gis-data. Wind turbine coordinates and their power and thrust curves are provided at https://zenodo.org/record/7374283#.Y4YZxC-B1KM. WRF namelists for NWF and WFP simulations may be acquired from https://zenodo.org/record/7374239#.Y4YaOy-B1KM. The NOW-23 simulation output data are available in HDF5 format at https://doi.org/10.25984/1821404.

6 Author contributions

Conceptualization: JKL, MO. Resources: MO, NB. Methodology: DR, JKL. Software: DR. Formal analysis and visualization: DR. Investigation: DR and JKL. Writing – original draft: DR and JKL. Writing – review and editing: all co-authors. Supervision: JKL.

7 Competing interests

At least one of the (co-)authors is a member of the editorial board of Wind Energy Science. Furthermore, Mike Optis co-authored the submitted manuscript while an employee of the National Renewable Energy Laboratory. He has since founded Veer Renewables, which recently released a wind modeling product, WakeMap, which is based on a similar numerical weather prediction modeling framework as the one described in this manuscript. Data from WakeMap is sold to wind energy stakeholders for profit. Public content on WakeMap include a website (https://veer.eco/wakemap/), a white paper (https://veer.eco/wp-content/uploads/2023/02/WakeMap_White_Paper_Veer_Renewables.pdf) and several LinkedIn posts promoting WakeMap. Mike Optis is the founder and president of Veer Renewables, a for-profit consulting company. Mike Optis is a shareholder of Veer Renewables and owns 92 % of its stock.

8 Acknowledgements

This work utilized the Alpine high-performance computing resource at the University of Colorado Boulder. Alpine is jointly funded by the University of Colorado Boulder, the University of Colorado Anschutz, and Colorado State University. Data storage supported by the University of Colorado Boulder 'PetaLibrary' A portion of this research was performed using computational resources sponsored by the DOE's Office of Energy Efficiency and Renewable Energy and located at NREL. This work was authored in part by the National Renewable Energy Laboratory, operated by Alliance for Sustainable Energy, LLC, for the US Department of Energy (DOE) under contract no. DE-AC36-08GO28308. Funding was provided by the US Department of Energy Office of Energy Efficiency and Renewable Energy Wind Energy Technologies Office. Support for the work was also provided by the National Offshore Wind Research and Development Consortium under agreement no. CRD-19-16351. The views expressed in the article do not necessarily represent the views of the DOE or the US Government. The US Government retains and the publisher, by accepting the article for publication, acknowledges that the US Government retains a nonexclusive, paid-up, irrevocable, worldwide license to publish or reproduce the published form of this work, or allow others to do so, for US Government purposes.

The authors wish to thank Louis Bowers and Sarah McElman for their questions that led to this line of inquiry.

9 Appendices

Appendix A

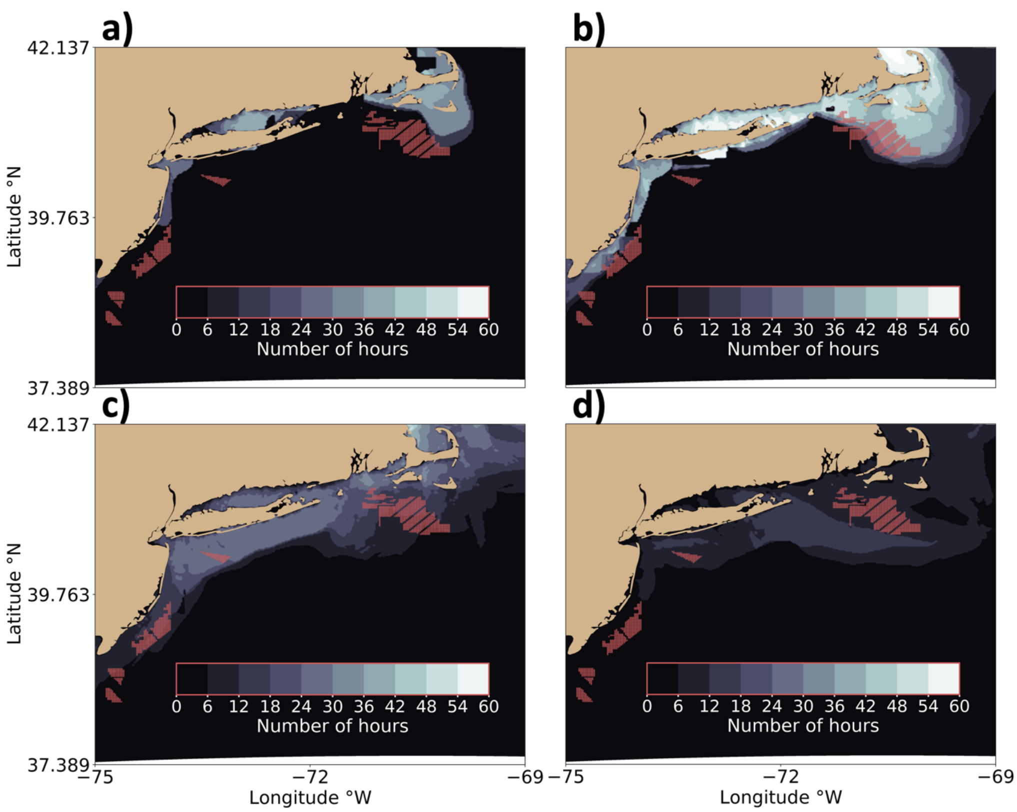

Figure. A1. The number of freezing hours at 10 m during (a) December 2019, (b) January 2020, (c) February 2020, and (d) March 2020. Lighter contouring indicates higher percentages. Red dots indicate turbine locations.

https://doi.org/10.5194/wes-2024-2
Preprint. Discussion started: 27 February 2024

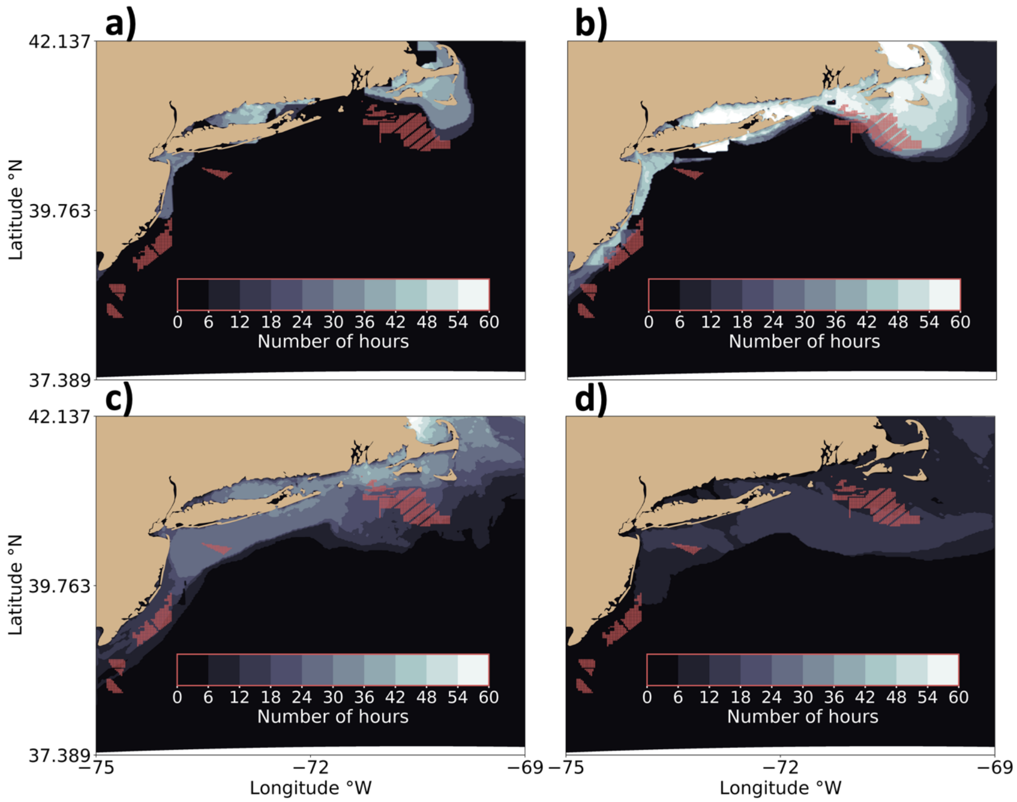

469

470 **Figure A2. The number of freezing hours at 20 m during (a) December 2019, (b) January 2020, (c) February 2020, and (d)**
471 **March 2020. Lighter contouring indicates higher percentages. Red dots indicate turbine locations.**

472

https://doi.org/10.5194/wes-2024-2
Preprint. Discussion started: 27 February 2024

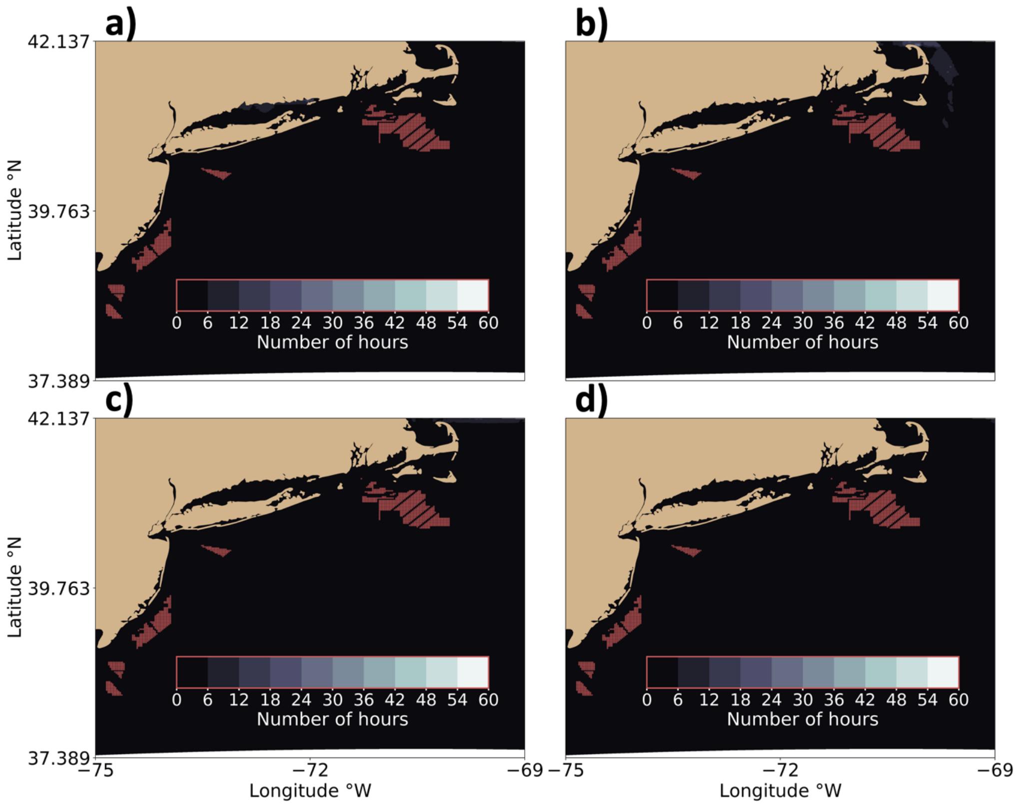

Figure A3. The number of freezing hours at hub height during (a) December 2019, (b) January 2020, (c) February 2020, and (d) March 2020. Lighter contouring indicates higher percentages. Note the color scheme is different from Supplementary Figs. 1 and 2. Red dots indicate turbine locations.

https://doi.org/10.5194/wes-2024-2
Preprint. Discussion started: 27 February 2024

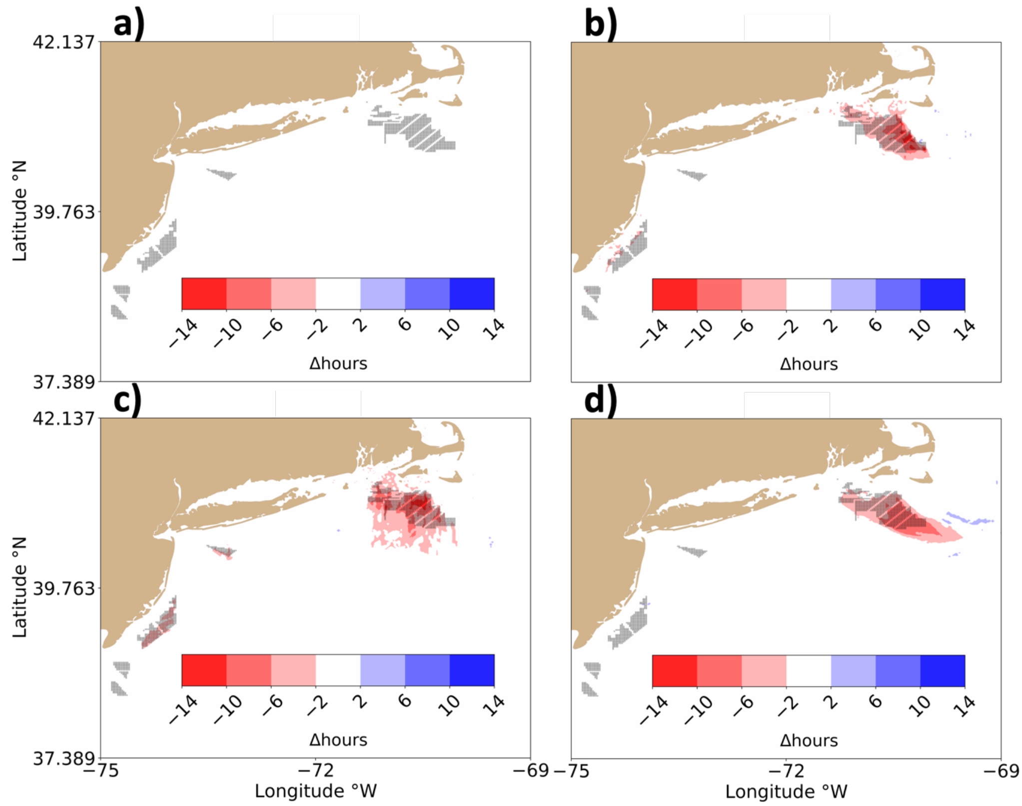

Figure A4. The (WFP-NWF) difference in freezing hours at 10 m during (a) December 2019, (b) January 2020, (c) February 2020, and (d) March 2020. Blue (red) contouring indicates higher (lower) percentages. Gray dots indicate turbine locations.

https://doi.org/10.5194/wes-2024-2
Preprint. Discussion started: 27 February 2024

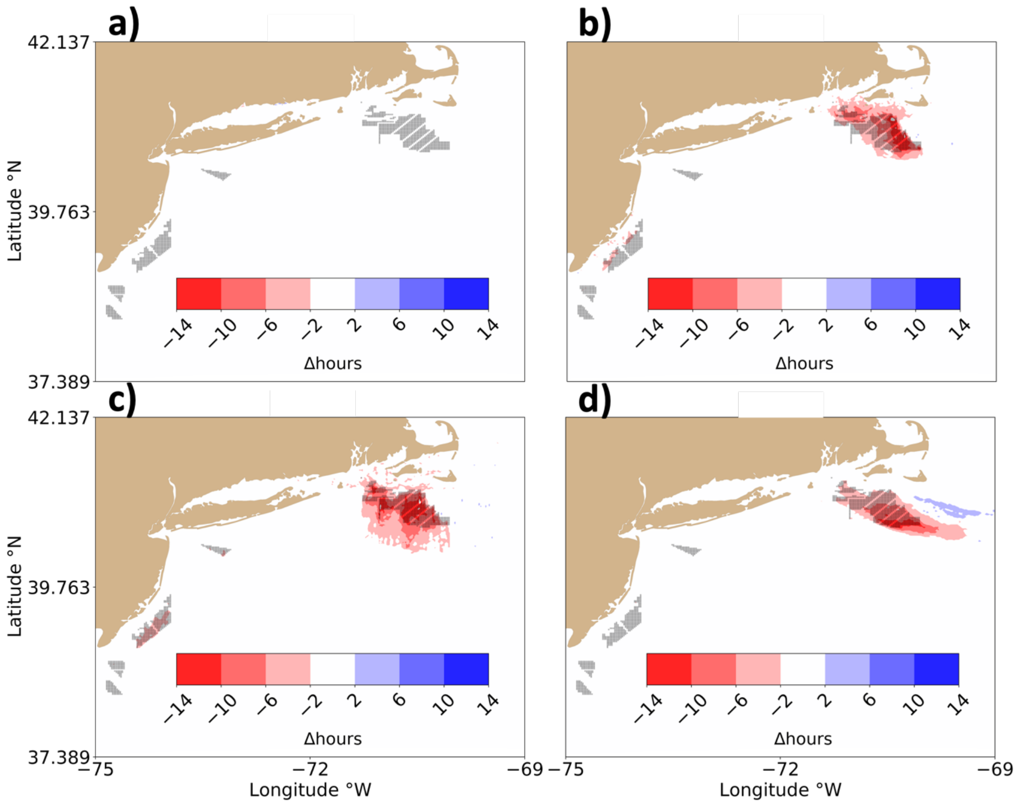

483

484 **Figure A5. The (WFP_0-NWF) difference in freezing hours at 20 m during (a) December 2019, (b) January 2020, (c)**
485 **February 2020, and (d) March 2020. Blue (red) contouring indicates higher (lower) percentages. Gray dots indicate**
486 **turbine locations.**

487

https://doi.org/10.5194/wes-2024-2
Preprint. Discussion started: 27 February 2024

eawe european academy of wind energy
Open Access WIND ENERGY SCIENCE DISCUSSIONS

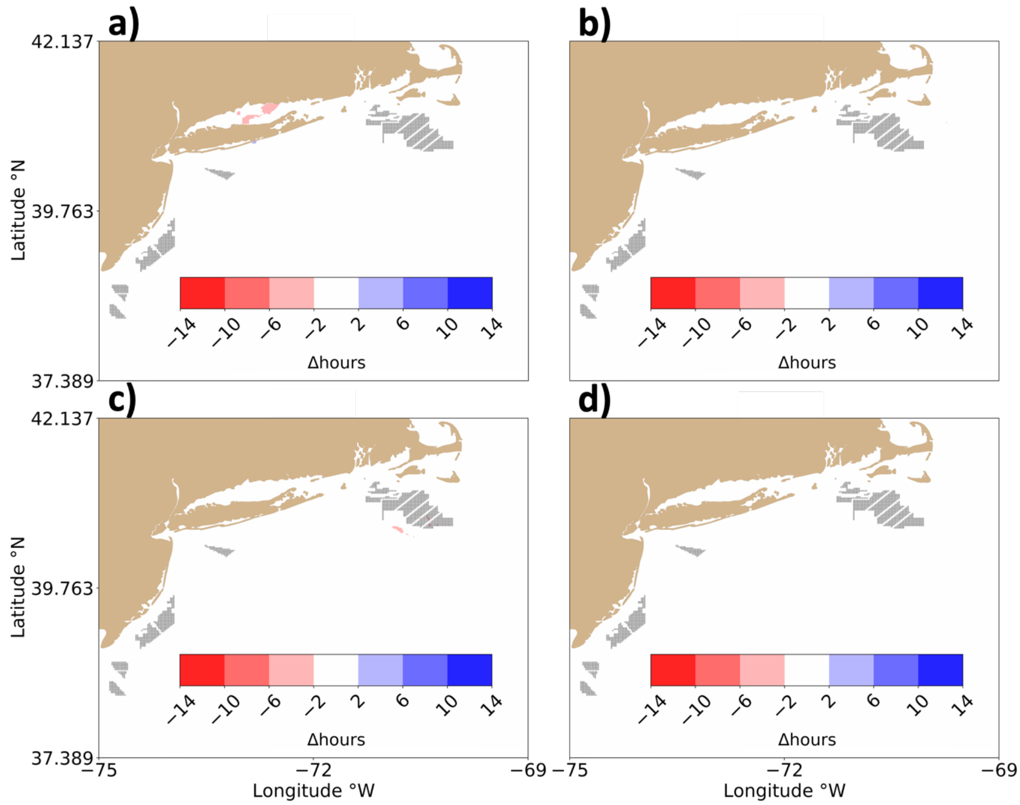

Figure A6. The (WFP-NWF) difference in freezing hours at the hub height during (a) December 2019, (b) January 2020, (c) February 2020, and (d) March 2020. Blue (red) contouring indicates higher (lower) percentages. Gray dots indicate turbine locations.

10 References

Ancell, B. C., Bogusz, A., Lauridsen, M. J., and Nauert, C. J.: Seeding Chaos: The Dire Consequences of Numerical Noise in NWP Perturbation Experiments, Bull. Amer. Meteor. Soc., 99, 615–628, https://doi.org/10.1175/BAMS-D-17-0129.1, 2018.

Archer, C. L., Colle, B. A., Veron, D. L., Veron, F., and Sienkiewicz, M. J.: On the predominance of unstable atmospheric conditions in the marine boundary layer offshore of the U.S. northeastern coast, Journal of Geophysical Research: Atmospheres, 121, 8869–8885, https://doi.org/10.1002/2016JD024896, 2016.

Archer, C. L., Wu, S., Ma, Y., and Jiménez, P. A.: Two Corrections for Turbulent Kinetic Energy Generated by Wind Farms in the WRF Model, Monthly Weather Review, 148, 4823–4835, https://doi.org/10.1175/MWR-D-20-0097.1, 2020.

Battisti, L., Fedrizzi, R., Brighenti, A., and Laakso, T.: Sea ice and icing risk for offshore wind turbines, Proceedings of the OWEMES, 20–22, https://citeseerx.ist.psu.edu/document?repid=rep1&type=pdf&doi=8bb110a8c86abf785b1b019dcc37150f09de90ae, 2006.

https://doi.org/10.5194/wes-2024-2
Preprint. Discussion started: 27 February 2024

Beiter, P., Musial, W., Duffy, P., Cooperman, A., Shields, M., Heimiller, D., and Optis, M.: The Cost of Floating Offshore Wind Energy in California Between 2019 and 2032, Renewable Energy, 113, https://doi.org/10.2172/1710181, 2020.

Bodini, N., Lundquist, J. K., and Kirincich, A.: U.S. East Coast Lidar Measurements Show Offshore Wind Turbines Will Encounter Very Low Atmospheric Turbulence, Geophysical Research Letters, 46, 5582–5591, https://doi.org/10.1029/2019GL082636, 2019.

Bodini, N., Optis, M., Redfern, S., Rosencrans, D., Rybchuk, A., Lundquist, J. K., Pronk, V., Castagneri, S., Purkayastha, A., Draxl, C., Krishnamurthy, R., Young, E., Roberts, B., Rosenlieb, E., and Musial, W.: The 2023 National Offshore Wind data set (NOW-23), Earth System Science Data Discussions, 1–57, https://doi.org/10.5194/essd-2023-490, 2023.

Cohen, J., Zhang, X., Francis, J., Jung, T., Kwok, R., Overland, J., Ballinger, T. J., Bhatt, U. S., Chen, H. W., Coumou, D., Feldstein, S., Gu, H., Handorf, D., Henderson, G., Ionita, M., Kretschmer, M., Laliberte, F., Lee, S., Linderholm, H. W., Maslowski, W., Peings, Y., Pfeiffer, K., Rigor, I., Semmler, T., Stroeve, J., Taylor, P. C., Vavrus, S., Vihma, T., Wang, S., Wendisch, M., Wu, Y., and Yoon, J.: Divergent consensuses on Arctic amplification influence on midlatitude severe winter weather, Nat. Clim. Chang., 10, 20–29, https://doi.org/10.1038/s41558-019-0662-y, 2020.

Contreras Montoya, L. T., Lain, S., and Ilinca, A.: A Review on the Estimation of Power Loss Due to Icing in Wind Turbines, Energies, 15, 1083, https://doi.org/10.3390/en15031083, 2022.

Dehghani-Sanij, A. R., Dehghani, S. R., Naterer, G. F., and Muzychka, Y. S.: Sea spray icing phenomena on marine vessels and offshore structures: Review and formulation, Ocean Engineering, 132, 25–39, https://doi.org/10.1016/j.oceaneng.2017.01.016, 2017.

Donlon, C. J., Martin, M., Stark, J., Roberts-Jones, J., Fiedler, E., and Wimmer, W.: The Operational Sea Surface Temperature and Sea Ice Analysis (OSTIA) system, Remote Sensing of Environment, 116, 140–158, https://doi.org/10.1016/j.rse.2010.10.017, 2012.

Ferrier, B. S., Jin, Y., Lin, Y., Black, T., Rogers, E., and DiMego, G.: Implementation of a new grid-scale cloud and precipitation scheme in the NCEP Eta model, Amer. Meteor. Soc. Conf. on Weather Analysis and Forecasting, 19, https://scholar.google.com/scholar?hl=en&as_sdt=0%2C6&q=Implementation+of+a+new+grid-scale+cloud+and+precipitation+scheme+in+the+NCEP+Eta+model&btnG=, 2002.

Fitch, A. C., Olson, J. B., Lundquist, J. K., Dudhia, J., Gupta, A. K., Michalakes, J., and Barstad, I.: Local and Mesoscale Impacts of Wind Farms as Parameterized in a Mesoscale NWP Model, Monthly Weather Review, 140, 3017–3038, https://doi.org/10.1175/MWR-D-11-00352.1, 2012.

Fitch, A. C., Lundquist, J. K., and Olson, J. B.: Mesoscale Influences of Wind Farms throughout a Diurnal Cycle, Mon. Wea. Rev., 141, 2173–2198, https://doi.org/10.1175/MWR-D-12-00185.1, 2013.

Gao, L. and Hong, J.: Wind turbine performance in natural icing environments: A field characterization, Cold Regions Science and Technology, 181, 103193, https://doi.org/10.1016/j.coldregions.2020.103193, 2021.

Gao, L. and Hu, H.: Wind turbine icing characteristics and icing-induced power losses to utility-scale wind turbines, Proceedings of the National Academy of Sciences, 118, e2111461118, https://doi.org/10.1073/pnas.2111461118, 2021.

Geerts, B., Giangrande, S. E., McFarquhar, G. M., Xue, L., Abel, S. J., Comstock, J. M., Crewell, S., DeMott, P. J., Ebell, K., Field, P., Hill, T. C. J., Hunzinger, A., Jensen, M. P., Johnson, K. L., Juliano, T. W., Kollias, P., Kosovic, B., Lackner, C., Luke, E., Lüpkes, C., Matthews, A. A., Neggers, R., Ovchinnikov, M., Powers, H., Shupe, M. D., Spengler, T., Swanson, B. E., Tjernström, M., Theisen, A. K., Wales, N. A., Wang, Y., Wendisch, M., and Wu, P.:

https://doi.org/10.5194/wes-2024-2
Preprint. Discussion started: 27 February 2024

eawe european academy of wind energy
Open Access WIND ENERGY SCIENCE DISCUSSIONS

The COMBLE Campaign: A Study of Marine Boundary Layer Clouds in Arctic Cold-Air Outbreaks, Bulletin of the American Meteorological Society, 103, E1371–E1389, https://doi.org/10.1175/BAMS-D-21-0044.1, 2022.

Golbazi, M., Archer, C. L., and Alessandrini, S.: Surface impacts of large offshore wind farms, Environ. Res. Lett., 17, 064021, https://doi.org/10.1088/1748-9326/ac6e49, 2022.

Guest, P. and Luke, R.: The Power of Wind and Water, Mariners Weather Log, https://www.vos.noaa.gov/MWL/dec_05/ves.shtml, 2005.

Hall, T. and Booth, J. F.: SynthETC: A Statistical Model for Severe Winter Storm Hazard on Eastern North America, Journal of Climate, 30, 5329–5343, https://doi.org/10.1175/JCLI-D-16-0711.1, 2017.

Hersbach, H., Bell, B., Berrisford, P., Hirahara, S., Horányi, A., Muñoz-Sabater, J., Nicolas, J., Peubey, C., Radu, R., Schepers, D., Simmons, A., Soci, C., Abdalla, S., Abellan, X., Balsamo, G., Bechtold, P., Biavati, G., Bidlot, J., Bonavita, M., De Chiara, G., Dahlgren, P., Dee, D., Diamantakis, M., Dragani, R., Flemming, J., Forbes, R., Fuentes, M., Geer, A., Haimberger, L., Healy, S., Hogan, R. J., Hólm, E., Janisková, M., Keeley, S., Laloyaux, P., Lopez, P., Lupu, C., Radnoti, G., de Rosnay, P., Rozum, I., Vamborg, F., Villaume, S., and Thépaut, J.-N.: The ERA5 global reanalysis, Quarterly Journal of the Royal Meteorological Society, 146, 1999–2049, https://doi.org/10.1002/qj.3803, 2020.

Hirsch, R. M., Slack, J. R., and Smith, R. A.: Techniques of trend analysis for monthly water quality data, Water Resources Research, https://doi.org/10.1029/WR018i001p00107, 1982.

Hussain, M. M. and Mahmud, I.: pyMannKendall: a python package for non parametric Mann Kendall family of trend tests., Journal of Open Source Software, 4, 1556, https://doi.org/10.21105/joss.01556, 2019.

Iacono, M. J., Delamere, J. S., Mlawer, E. J., Shephard, M. W., Clough, S. A., and Collins, W. D.: Radiative forcing by long-lived greenhouse gases: Calculations with the AER radiative transfer models, Journal of Geophysical Research: Atmospheres, 113, https://doi.org/10.1029/2008JD009944, 2008.

Kain, J. S.: The Kain–Fritsch Convective Parameterization: An Update, Journal of Applied Meteorology and Climatology, 43, 170–181, https://doi.org/10.1175/1520-0450(2004)043<0170:TKCPAU>2.0.CO;2, 2004.

Destination likely sank after accumulating ice in heavy freezing spray, report says: https://www.ktoo.org/2018/07/16/destination-likely-sank-after-accumulating-ice-in-heavy-freezing-spray-report-says/, last access: 12 April 2023.

Kraj, A. G. and Bibeau, E. L.: Phases of icing on wind turbine blades characterized by ice accumulation, Renewable Energy, 35, 966–972, https://doi.org/10.1016/j.renene.2009.09.013, 2010.

Lauridsen, M. J. and Ancell, B. C.: Nonlocal Inadvertent Weather Modification Associated with Wind Farms in the Central United States, Advances in Meteorology, 2018, e2469683, https://doi.org/10.1155/2018/2469683, 2018.

Line, W. E., Grasso, L., Hillger, D., Dierking, C., Jacobs, A., and Shea, S.: Using NOAA Satellite Imagery to Detect and Track Hazardous Sea Spray in the High Latitudes, Weather and Forecasting, 37, 351–369, https://doi.org/10.1175/WAF-D-21-0137.1, 2022.

NTSB announces the probable cause of the sunken Scandies Rose: https://www.alaskasnewssource.com/2021/06/29/ntsb-announce-probable-cause-sunken-scandies-rose/, last access: 12 April 2023.

Madi, E., Pope, K., Huang, W., and Iqbal, T.: A review of integrating ice detection and mitigation for wind turbine blades, Renewable and Sustainable Energy Reviews, 103, 269–281, https://doi.org/10.1016/j.rser.2018.12.019, 2019.

https://doi.org/10.5194/wes-2024-2
Preprint. Discussion started: 27 February 2024

Martini, F., Contreras Montoya, L. T., and Ilinca, A.: Review of Wind Turbine Icing Modelling Approaches, Energies, 14, 5207, https://doi.org/10.3390/en14165207, 2021.

Monin, A. S. and Obukhov, A. M.: Basic laws of turbulent mixing in the surface layer of the atmosphere, Tr. Akad. Nauk SSSR Geophiz. Inst., 24, 30, https://gibbs.science/efd/handouts/monin_obukhov_1954.pdf, 1954.

Nakanishi, M. and Niino, H.: An Improved Mellor–Yamada Level-3 Model: Its Numerical Stability and Application to a Regional Prediction of Advection Fog, Boundary-Layer Meteorol, 119, 397–407, https://doi.org/10.1007/s10546-005-9030-8, 2006.

Icing believed to cause sinking of fishing boat in Barents Sea, 17 missing: https://thebarentsobserver.com/en/2020/12/icing-believed-cause-sining-fishing-boat-barents-sea-17-missing, last access: 12 April 2023.

Niu, G.-Y., Yang, Z.-L., Mitchell, K. E., Chen, F., Ek, M. B., Barlage, M., Kumar, A., Manning, K., Niyogi, D., Rosero, E., Tewari, M., and Xia, Y.: The community Noah land surface model with multiparameterization options (Noah-MP): 1. Model description and evaluation with local-scale measurements, Journal of Geophysical Research: Atmospheres, 116, https://doi.org/10.1029/2010JD015139, 2011.

Novacheck, J., Sharp, J., Schwarz, M., Donohoo-Vallett, P., Tzavelis, Z., Buster, G., and Rossol, M.: The Evolving Role of Extreme Weather Events in the U.S. Power System with High Levels of Variable Renewable Energy, NREL/TP-6A20-78394, 1837959, MainId:32311, NREL/TP-6A20-78394, 1837959, MainId:32311, https://doi.org/10.2172/1837959, 2021.

NREL: 2023 National Offshore Wind data set (NOW-23), https://dx.doi.org/10.25984/1821404, 2020.

Glossary - NOAA's National Weather Service: https://w1.weather.gov/glossary/index.php?word=freezing+spray, last access: 12 April 2023.

Nygaard, N. G.: Wakes in very large wind farms and the effect of neighbouring wind farms, J. Phys.: Conf. Ser., 524, 012162, https://doi.org/10.1088/1742-6596/524/1/012162, 2014.

Overland, J. E.: Prediction of Vessel Icing for Near-Freezing Sea Temperatures, Weather and Forecasting, 5, 62–77, https://doi.org/10.1175/1520-0434(1990)005<0062:POVIFN>2.0.CO;2, 1990.

Overland, J. E., Pease, C. H., Preisendorfer, R. W., and Comiskey, A. L.: Prediction of Vessel Icing, Journal of Applied Meteorology and Climatology, 25, 1793–1806, https://doi.org/10.1175/1520-0450(1986)025<1793:POVI>2.0.CO;2, 1986.

Parish, T. R., Burkhart, M. D., and Rodi, A. R.: Determination of the Horizontal Pressure Gradient Force Using Global Positioning System on board an Instrumented Aircraft, Journal of Atmospheric and Oceanic Technology, 24, 521–528, https://doi.org/10.1175/JTECH1986.1, 2007.

Platis, A., Siedersleben, S. K., Bange, J., Lampert, A., Bärfuss, K., Hankers, R., Cañadillas, B., Foreman, R., Schulz-Stellenfleth, J., Djath, B., Neumann, T., and Emeis, S.: First in situ evidence of wakes in the far field behind offshore wind farms, Sci Rep, 8, 2163, https://doi.org/10.1038/s41598-018-20389-y, 2018.

Powers, J. G., Klemp, J. B., Skamarock, W. C., Davis, C. A., Dudhia, J., Gill, D. O., Coen, J. L., Gochis, D. J., Ahmadov, R., Peckham, S. E., Grell, G. A., Michalakes, J., Trahan, S., Benjamin, S. G., Alexander, C. R., Dimego, G. J., Wang, W., Schwartz, C. S., Romine, G. S., Liu, Z., Snyder, C., Chen, F., Barlage, M. J., Yu, W., and Duda, M. G.: The Weather Research and Forecasting Model: Overview, System Efforts, and Future Directions, Bulletin of the American Meteorological Society, 98, 1717–1737, https://doi.org/10.1175/BAMS-D-15-00308.1, 2017.

https://doi.org/10.5194/wes-2024-2
Preprint. Discussion started: 27 February 2024

Pronk, V., Bodini, N., Optis, M., Lundquist, J. K., Moriarty, P., Draxl, C., Purkayastha, A., and Young, E.: Can reanalysis products outperform mesoscale numerical weather prediction models in modeling the wind resource in simple terrain?, Wind Energ. Sci., 7, 487–504, https://doi.org/10.5194/wes-7-487-2022, 2022.

Rajewski, D. A., Takle, E. S., Lundquist, J. K., Oncley, S., Prueger, J. H., Horst, T. W., Rhodes, M. E., Pfeiffer, R., Hatfield, J. L., Spoth, K. K., and Doorenbos, R. K.: Crop Wind Energy Experiment (CWEX): Observations of Surface-Layer, Boundary Layer, and Mesoscale Interactions with a Wind Farm, Bulletin of the American Meteorological Society, 94, 655–672, https://doi.org/10.1175/BAMS-D-11-00240.1, 2013.

Redfern, S., Optis, M., Xia, G., and Draxl, C.: Offshore wind energy forecasting sensitivity to sea surface temperature input in the Mid-Atlantic, Wind Energy Science, 8, 1–23, https://doi.org/10.5194/wes-8-1-2023, 2023.

Rosencrans, D., Lundquist, J. K., Optis, M., Rybchuk, A., Bodini, N., and Rossol, M.: Annual Variability of Wake Impacts on Mid-Atlantic Offshore Wind Plant Deployments [preprint], Wind Energy Science Discussions, 1–39, https://doi.org/10.5194/wes-2023-38, 2023.

Russell, L. M.: Sea-spray particles cause freezing in clouds, Nature, 525, 194–195, https://doi.org/10.1038/525194a, 2015.

Schneemann, J., Rott, A., Dörenkämper, M., Steinfeld, G., and Kühn, M.: Cluster wakes impact on a far-distant offshore wind farm's power, Wind Energy Science, 5, 29–49, https://doi.org/10.5194/wes-5-29-2020, 2020.

Shcherbina, A. Y. and Gawarkiewicz, G. G.: A coastal current in winter: 2. Wind forcing and cooling of a coastal current east of Cape Cod, Journal of Geophysical Research: Oceans, 113, https://doi.org/10.1029/2008JC004750, 2008a.

Shcherbina, A. Y. and Gawarkiewicz, G. G.: A coastal current in winter: Autonomous underwater vehicle observations of the coastal current east of Cape Cod, Journal of Geophysical Research: Oceans, 113, https://doi.org/10.1029/2007JC004306, 2008b.

Siedersleben, S. K., Lundquist, J. K., Platis, A., Bange, J., Bärfuss, K., Lampert, A., Cañadillas, B., Neumann, T., and Emeis, S.: Micrometeorological impacts of offshore wind farms as seen in observations and simulations, Environ. Res. Lett., 13, 124012, https://doi.org/10.1088/1748-9326/aaea0b, 2018.

Stoelinga, M., Sanchez-Gomez, M., Poulos, G. S., and Crescenti, J.: Estimating Long-Range External Wake Losses in Energy Yield and Operational Performance Assessments Using the WRF Wind Farm Parameterization, 20, https://arcvera.com/wp-content/uploads/2022/08/ArcVera-White-Paper-Estimating-Long-Range-External-Wake-Losses-WRF-WFP-1.0.pdf, 2022.

SWAN Team: Scientific and Technical Documentation (SWAN Cycle III version 41.31A), Delft University of Technology, https://swanmodel.sourceforge.io/download/zip/swantech.pdf, 2020.

Tewari, M., Chen, F., Wang, W., Dudhia, J., LeMone, M., Mitchell, K., Ek, M., Gayno, G., Wegiel, J., and Cuenca, R. H.: (PDF) Implementation and verification of the united NOAH land surface model in the WRF model, Proceedings of the 20th conference on weather analysis and forecasting/16th conference on numerical weather prediction, 14, https://www.researchgate.net/publication/286272692_Implementation_and_verification_of_the_united_NOAH_land_surface_model_in_the_WRF_model, 2004.

Thompson, G., Field, P. R., Rasmussen, R. M., and Hall, W. D.: Explicit Forecasts of Winter Precipitation Using an Improved Bulk Microphysics Scheme. Part II: Implementation of a New Snow Parameterization, Monthly Weather Review, 136, 5095–5115, https://doi.org/10.1175/2008MWR2387.1, 2008.

Tolman, H., Abdolali, A., Accensi, M., Alves, J.-H., Ardhuin, F., Babanin, A., Barbariol, F., Benetazzo, A., Bidlot, J., Booij, N., Boutin, G., Bunney, C., Campbell, T., Chalikov, D., Chawla, A., Cheng, S., Collins III, C., Filipot, J.-

F., Flampouris, S., and Liang, Z.: User manual and system documentation of WAVEWATCH III (R) version 6.07, https://www.researchgate.net/publication/336069899_User_manual_and_system_documentation_of_WAVEWATCH_III_R_version_607, 2019.

Tomaszewski, J. M. and Lundquist, J. K.: Simulated wind farm wake sensitivity to configuration choices in the Weather Research and Forecasting model version 3.8.1, Geoscientific Model Development, 13, 2645–2662, https://doi.org/10.5194/gmd-13-2645-2020, 2020.

Vavrus, S., Walsh, J. E., Chapman, W. L., and Portis, D.: The behavior of extreme cold air outbreaks under greenhouse warming, International Journal of Climatology, 26, 1133–1147, https://doi.org/10.1002/joc.1301, 2006.

Wei, K., Yang, Y., Zuo, H., and Zhong, D.: A review on ice detection technology and ice elimination technology for wind turbine, Wind Energy, 23, 433–457, https://doi.org/10.1002/we.2427, 2020.

FACT SHEET: Biden Administration Jumpstarts Offshore Wind Energy Projects to Create Jobs: https://www.whitehouse.gov/briefing-room/statements-releases/2021/03/29/fact-sheet-biden-administration-jumpstarts-offshore-wind-energy-projects-to-create-jobs/, last access: 4 April 2023.

Winters, A. C., Bosart, L. F., and Keyser, D.: Antecedent North Pacific Jet Regimes Conducive to the Development of Continental U.S. Extreme Temperature Events during the Cool Season, Weather and Forecasting, 34, 393–414, https://doi.org/10.1175/WAF-D-18-0168.1, 2019.

Xia, G., Zhou, L., Freedman, J. M., Roy, S. B., Harris, R. A., and Cervarich, M. C.: A case study of effects of atmospheric boundary layer turbulence, wind speed, and stability on wind farm induced temperature changes using observations from a field campaign, Clim Dyn, 46, 2179–2196, https://doi.org/10.1007/s00382-015-2696-9, 2016.